18

Magnetospheric Model Performance during Conjugate Aurora

William Longley[1], Patricia Reiff[1], Jone Peter Reistad[2], and Nikolai Østgaard[2]

Video of Yosemite Talk, URL: http://dx.doi.org/10.15142/T3H01C

ABSTRACT

On 17 August 2001, the Imager for Magnetopause-to-Aurora Global Explorer (IMAGE) satellite viewed the Northern aurora, while the POLAR satellite observed the Southern aurora. Unlike typical cases where the aurora is conjugate, the large Y-component of the Interplanetary Magnetic Field (IMF) makes the polar cap shift toward the dusk in one hemisphere and toward the dawn in the other. Using the satellite images, we identified the Polar Cap Boundary (PCB) in both hemispheres, and determined the Dawn-Dusk Offset, ΔL, which ranged from 0° to 15° latitude. We found correlations of 0.90 in the North and 0.83 in the South between ΔL and IMF By. We then computed PCBs using four magnetohydrodynamic (MHD) models. None of the models accurately reproduced the observations, with Block Adaptive Tree Solar Wind Roe-type Upwind Scheme (BATS-R-US) producing boundaries that are too symmetric, Open Geospace General Circulation Model (OpenGGCM) producing boundaries that are too distorted, and the LFM-MIX model giving the best average offset but did not match the observed variation with solar wind parameters.

18.1. INTRODUCTION

The aurora is a highly visible indicator of magnetosphere-ionosphere coupling. We use the auroral response of a coronal mass ejection (CME) to test magnetospheric MHD models. The purpose of this study is not to perform a careful optimization of the models but instead to take the "standard" versions of the Community Coordinated Modeling Center (CCMC) models, which are in heavy use among the community and challenge them with unusual input conditions, to see which performs best. The CME carried a strong magnetic field, with a y-component (By) averaging 25 nT for nearly 12 hours and a z-component (Bz) varying from 0 nT to −20 nT. During this time span, the Kp index peaked at 7, and aurora were simultaneously observed by IMAGE in the northern hemisphere, and by POLAR in the southern hemisphere.

In 1996 POLAR was launched in a highly elliptical polar orbit with an 18-hour period, spending 13 hours of the orbit imaging the aurora in one hemisphere [*Frank et. al,* 1995]. By 2001, the apogee of the orbit was above the equator and allowed POLAR to start observing the aurora in the southern hemisphere for several hours at a time. The IMAGE satellite was launched in early 2000 and placed into a highly elliptical polar orbit, spending 10 hours of its 14.2-hour orbital period high above the northern hemisphere [*Burch,* 2000]. The precession of each satellite's orbit from the northern hemisphere to the southern led to a brief window from 2001 to 2002 where each satellite was able to concurrently observe a different hemisphere.

[1]*Department of Physics and Astronomy, Rice University, Houston, TX, USA*

[2]*Department of Physics and Technology, University of Bergen, Bergen, Norway*

Magnetosphere-Ionosphere Coupling in the Solar System, Geophysical Monograph 222, First Edition.
Edited by Charles R. Chappell, Robert W. Schunk, Peter M. Banks, James L. Burch, and Richard M. Thorne.

Trapped particles in Earth's magnetic field will follow field lines and bounce between the north and south hemispheres, eventually precipitating into the atmosphere and creating the aurora when the particles are scattered or accelerated into the "loss cone" [*Reiff et al.,* 1988]. *Østgaard et al.* [2005] used simultaneous conjugate aurora events observed by POLAR and IMAGE to identify shared features of the aurora in each hemisphere. The distinct features were found to be shifted in longitude, an effect present in runs of the Tsyganenko 96 and 02 models during the same events. *Liou and Newell* [2010] used POLAR data to determine the longitude of 2539 auroral breakups, which were found to correlate well with the By component of the IMF and the dipole tilt angle. Similarly, *Stubbs et al.* [2005] found effects of the IMF on non-conjugacy of auroral images.

18.2. DATA ANALYSIS

18.2.1. Coordinate Systems

Our examination of the aurora requires two different coordinate systems: one three-axis Cartesian system to measure components of the IMF, and one latitude and longitude system to create polar plots of the aurora. To measure the IMF, we use the Geocentric Solar Magnetospheric (GSM) coordinate system defined by the x-axis lying along the Sun-Earth line, the z-axis containing the projection of the magnetic dipole orthogonal to the x-axis, and the y-axis completing the right-handed orthogonal triad [*Hapgood,* 1992].

The raw data from IMAGE and POLAR capture whatever the camera is pointing at. To make these data comparable between satellites, and even successive time steps of the same satellite, we map it to a latitude- and longitude-based polar map. The Apex coordinate system is well suited for mapping where the aurora occur, and is based on magnetic shells, where each magnetic shell has an apex of a given height above the Earth's surface [*VanZandt et al.,* 1972]. The latitude in the Apex coordinate system specifies the magnetic shell the point lies on, and the longitude specifies the Magnetic Local Time (MLT) of the particular field line. The third Apex coordinate specifies the height above the Earth, and we take that coordinate to be the 100 km ionosphere boundary when mapping the aurora.

18.2.2. Auroral Imaging Data

The IMAGE satellite was in position to capture the 17 August 2001 event in the northern hemisphere from 16:41 Universal Time (UT) to 19:01 UT. The Far Ultra Violet Imager/Wideband Imaging Camera (FUV/WIC) instrument is used to view the aurora in the 140 nm to 190 nm ultraviolet band, capturing several Nitrogen emission lines in the Lyman-Birge-Hopfield band and a few atomic Nitrogen lines [*Mende et al.,* 2000]. WIC has an angular resolution of 0.1 degrees and a temporal resolution of 123 seconds [*Burch,* 2000]. The POLAR satellite was able to fully capture the event in the southern hemisphere from 17:00 UT to 18:13 UT and captured the nightside of the event during the remainder of the 16:41 UT to 19:01 UT window. The visible (VIS) Earth instrument measures the 130.4 nm Oxygen emission line with a spatial resolution of 0.12 degrees [*Frank et. al,* 1995]. POLAR-VIS has a temporal resolution of 54 seconds, but the 2-min temporal resolution of IMAGE is used instead, matched to the closest POLAR image. Figure 18.1 shows a snapshot at 18:38 UT of the dataset used, with a lobe cell convection pattern overlaid onto the northern hemisphere [*Reiff et al.,* 1985].

We identify the PCB in the images by using an operational definition of a 2.0 kR (1300 counts on the detector) precipitation threshold for IMAGE data, and a 6.0 kR (27 counts on the detector) precipitation threshold for POLAR data. The Dawn-Dusk Offset, ΔL, is then computed by subtracting the colatitude of the PCB at 6:00 MLT from the colatitude of the PCB at 18:00 MLT. Positive ΔL values signify a polar cap that is shifted to the dusk, and negative ΔL values signify a polar cap shifted to the dawn. For instances where a satellite does not completely capture the aurora at 6:00 or 18:00 MLT, we estimate the location of the PCB and place an appropriately sized error bar on that point. For all points a minimum error of $\pm$0.3 degrees latitude is used to account for the pixel width of the data. For the 67 image frames we use, 1 of the frames from IMAGE does not capture the 18:00 MLT boundary, 3 of the frames from POLAR fail to capture both the 6:00 MLT boundary and the 18:00 MLT boundary, and 24 of the POLAR frames only capture the 6:00 boundary. Note that using a higher value of the auroral brightness for the operational definition of the PCB will yield a lower (and more circular) PCB. This will be explored in a second paper in progress.

18.2.3. Models

The results from the IMAGE and POLAR observations are compared to the outputs of the Space Weather Modeling Framework (SWMF)/BATS-R-US model both with and without the Comprehensive Ring Current Model (referred to as BATS-R-US and BATS-CRCM from here on) [*Glocer et al.,* 2013; *Tóth et al.,* 2012], the OpenGGCM model [*Raeder et al.,* 2001; *Fuller-Rowell et al.,* 1996], and the CMIT/LFM-MIX model (referred to as LFM) [*Lyon et al.,* 2004; *Merkin and Lyon,* 2010]. All models were run from the CCMC website, using the measured solar wind plasma and

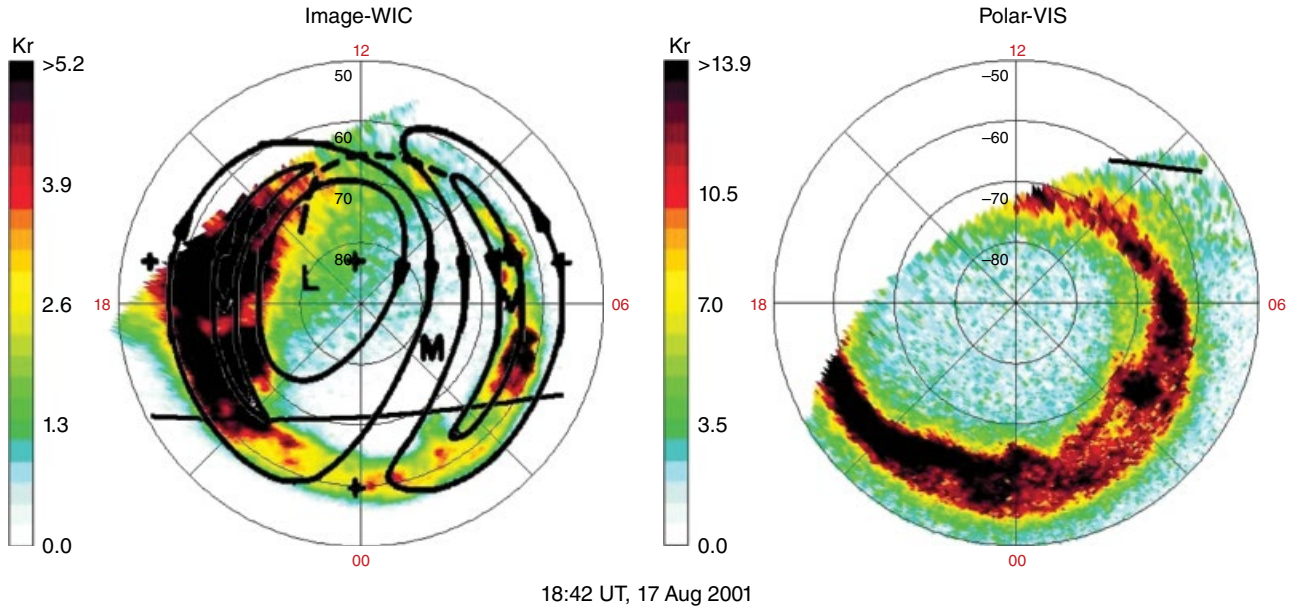

Figure 18.1 The aurora observed by IMAGE in the northern hemisphere and by POLAR in the southern hemisphere at 18:38 UT. The northern polar cap shows a shift toward dawn, and the southern hemisphere shows a clear shift toward dusk. In these images looking down on the Apex pole, noon is at the top and dawn is at the right. A lobe cell convection pattern [adapted from *Reiff et al.*, 1985] has been overlaid on the northern hemisphere auroral image.

magnetic field as inputs to solve three-dimensional MHD equations. Each model approximates the Earth's magnetic field as a dipole, with the BATS-R-US models allowing the dipole tilt angle to update throughout the simulation, and the OpenGGCM and LFM models keeping a fixed dipole tilt angle for the duration of the run. The BATS-R-US, BATS-CRCM, and OpenGGCM models use a 5.4 nT average Bx over the course of the model run, while the LFM model only allows 0 Bx. The BATS-CRCM and LFM models are coupled to inner magnetosphere models (CRCM and MIX, respectively). Both the BATS-R-US and the BATS-CRCM were run in higher resolution mode for the inner boundary. The models were run from 16:15 to 19:15 UT to minimize the effects of a fixed dipole tilt in the OpenGGCM and LFM models. *Pulkkinen et al.* [2013] provides more in-depth comparisons and descriptions of the models used.

The PCB is an output of each model run, and is obtained by tracing field lines to determine the open-closed boundary in the model. The boundary is plotted on the ionosphere map, which can be seen in Figure 18.2. For each frame of the ionosphere the Dawn-Dusk Offset, ΔL, is computed in the same way we computed ΔL for the IMAGE and POLAR data. Some of the outputs of the OpenGGCM and LFM models have multi-valued boundaries at a fixed MLT. We handle this in two ways. The first way is to locate and record each distinct value of the PCB at the desired MLT, and to then independently examine each point's evolution in time. The second way is to average all the locations together, compute the standard deviation, and then use that standard deviation as an error bar for our analysis.

18.2.4. Solar Wind Data

We use the "OMNI 1 minute IMF and Plasma data" dataset from CDAWeb for our IMF and solar wind data. The IMF and solar wind data are already time shifted to account for propagation to the Earth's bow shock and are averaged over 1-min intervals. The key parameters used for plots are the IMF By and Bz components in GSM coordinates; the IMF Clock Angle, $\theta_C = \text{Arctan}(By/Bz)$; and the Epsilon parameter, $\varepsilon = vB^2 \text{Sin}^4(\theta_C/2)$. Figure 18.3 shows By, Bz, and θ_C parameters during the event, as well as one hour prior to the event.

18.3. RESULTS

The computed Dawn-Dusk Offset observed by the IMAGE and POLAR satellites is plotted against the solar wind parameters By, θ_C, and ε (not shown). We perform a least squares fit to account for the error bar, σ, associated with each point ΔL, and then compute the standard correlation coefficient r. We use the ΔL and σ values from each frame of data to calculate the fit; therefore, a ΔL value with a large error will be unimportant to the fit line.

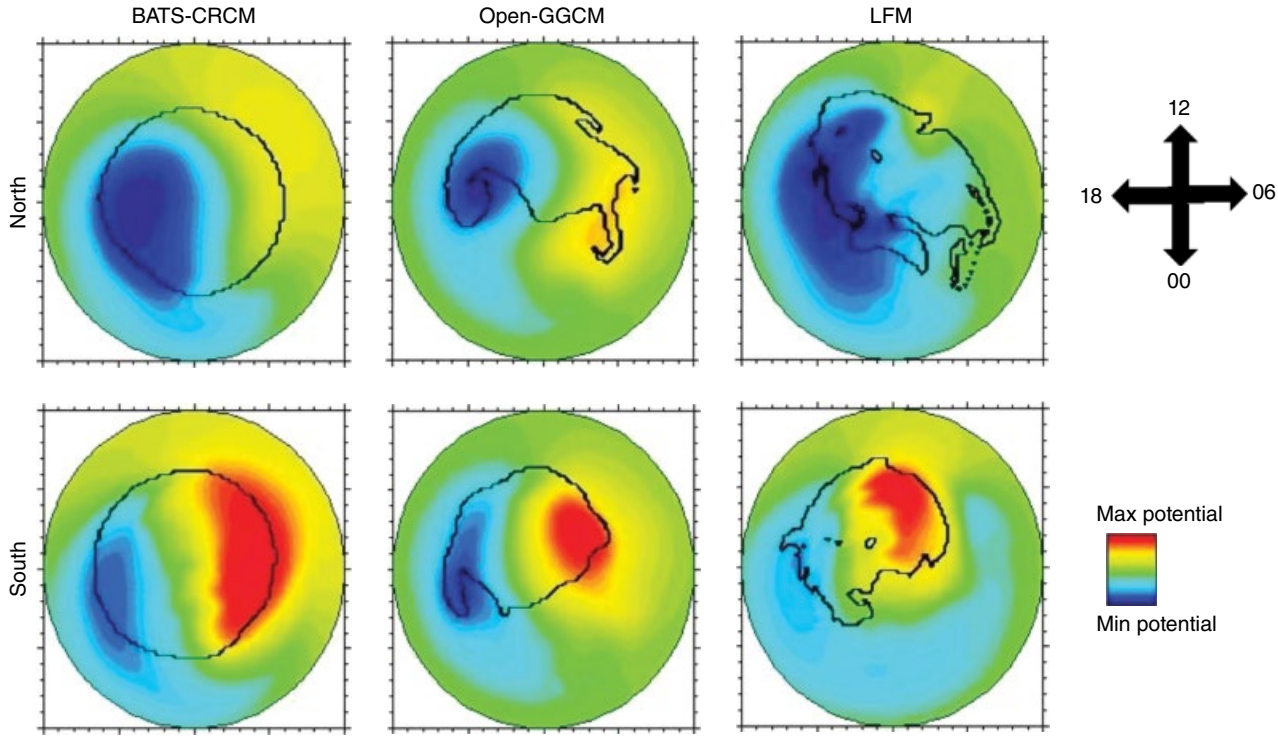

Figure 18.2 Ionosphere and polar cap boundary at 18:41 UT for various models. The color indicates the ionospheric potential, and the solid circle indicates the polar cap boundary (which is distorted for some of the models at certain times). The blue area is convection flowing clockwise, and the red area is convection flowing counterclockwise. In steady state, flow lines are equipotentials. Not shown is the BATS-R-US plot, which is nearly identical to the BATS-CRCM plot.

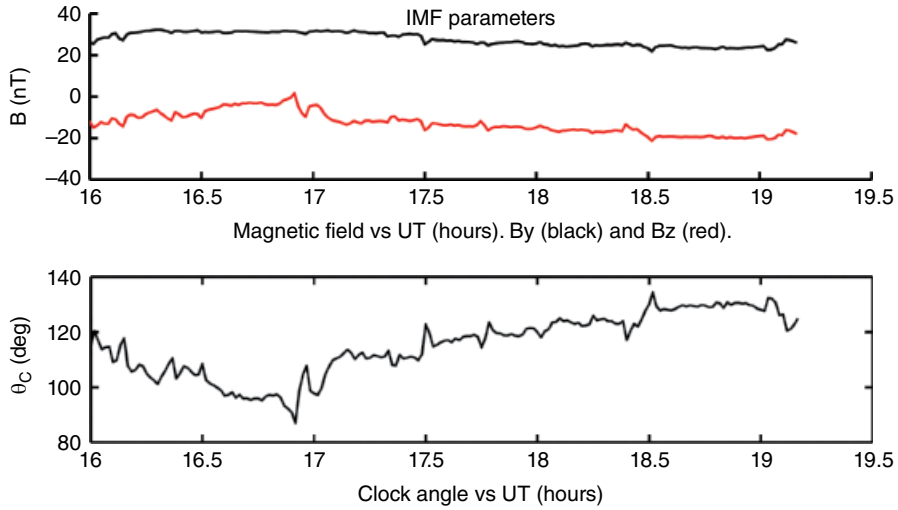

Figure 18.3 Top, IMF B_y (black) and B_z (red). Bottom, Clock Angle (θ_C) on 17 August 2001.

When calculating the correlation coefficient, we only include ΔL values where σ is less than 2 degrees of latitude (which excludes 5 of the 67 data points). Taking the 1-min averaged solar wind parameters, we find the Dawn-Dusk Offset, ΔL, correlates best with By in both hemispheres, with $r = 0.84$ in the north and $r = 0.81$ in the south. Table 18.1 shows the correlations of ΔL with θ_C and ε.

The Earth's magnetosphere has been shown to reconfigure over a 30- to 60-min window in response to changes in the solar wind. To explore this expectation we use time

Table 18.1 Correlations (r) of various solar wind parameters against the observed Dawn-Dusk Offset from the IMAGE and POLAR satellites. Correlations listed as Northern Hemisphere, (Southern Hemisphere). For each function, the time shown in the second column is for the best correlation

	1 min By	30 min $<B_y>$	1 min θ_C	45 min $<\theta_C>$	1 min ε	50 min $<\varepsilon>$
ΔL	0.84 (0.81)	0.90 (0.83)	−0.79 (−0.68)	−0.88 (−0.85)	0.73 (0.56)	−0.85 (−0.87)

Table 18.2 Correlations (r) of 30 min averaged B_y against the Dawn-Dusk Offset (ΔL) as determined by each of the models. Correlations (r) of a 45 min averaged θ_C against ΔL also shown in parentheses for comparison

	BATS-R-US	BATS-CRCM	OpenGGCM Poleward	OpenGGCM Equator	LFM Poleward	LFM Equator
ΔL in North	−0.75 (0.75)	−0.91 (0.92)	−0.42 (0.45)	0.44 (−0.43)	−0.29 (0.21)	−0.30 (−0.35)
ΔL in South	0.11 (−0.11)	0.31 (−0.32)	0 (0)	0.24 (−0.27)	0.48 (−0.49)	0.11 (−0.05)

Table 18.3 Minimum and maximum Dawn-Dusk Offsets from every satellite and model (in degrees of latitude)

Northern Hemisphere	IMAGE	BATS-R-US	BATS-CRCM	OpenGGCM Poleward	OpenGGCM Equator	LFM Poleward	LFM Equator
Average ΔL	−7.6°	−2.2°	−0.6°	−6.1°	−4.4°	−10.4°	1.7°
(Min, Max) ΔL	(−15°, 0°)	(−4°, −1°)	(−4°, 1°)	(−15°, 12°)	(−18°, 20°)	(−21°, −5°)	(−2°, 8°)
Southern Hemisphere	POLAR	BATS-R-US	BATS-CRCM	OpenGGCM Poleward	OpenGGCM Equator	LFM Poleward	LFM Equator
Average ΔL	10.2°	2.5°	5°	3.7°	14.4°	14.5°	15.3°
(Min, Max) ΔL	(5°, 14°)	(2°, 3°)	(4°, 7°)	(−10°, 21°)	(2°, 31°)	(8°, 19°)	(13°, 19°)

averages of By, θ_C, and ε. A constant weighted average of the parameters over the previous *t* minutes works best, and by trying different values of *t* we can improve the correlations of ΔL against each of the three solar wind parameters. For By, we find a 30-min constant average produces the best correlations, with r = 0.90 in the northern hemisphere and r = 0.83 in the southern hemisphere. Table 18.1 shows the correlations of all the time-averaged parameters.

18.4. MODEL RESULTS

Using the same methods from Section 18.3, we check the correlation of ΔL as calculated by the MHD models against the solar wind parameters By, and θ_C. The correlation coefficients from these plots are listed in Table 18.2. Since the OpenGGCM and LFM models have PCBs that are often multivalued along a given meridian, we have tracked the polar cap at both the lowest (listed as equator, since this is the most equatorward boundary) and highest (listed as poleward, as this is the most poleward boundary) latitudes that it crosses the dawn-dusk meridian. Both BATS models show strong correlations with ΔL in the northern hemisphere, with the CRCM inner magnetosphere model improving the correlations in all cases. However, the BATS models disagree with the satellite data in the northern hemisphere on the sign of the correlation; when ΔL is increasing in the data, it is decreasing in the models.

What is more useful, and more interesting, is comparing the plot trends between each model. Table 18.3 lists the ranges and average of ΔL in each hemisphere for all the models and the satellite data. Both BATS-R-US models have very small Dawn-Dusk Offsets, whereas the POLAR/IMAGE data, the LFM model, and the OpenGGCM model all have abs(ΔL) > 10° at times, and a large range of ΔL over the course of the event. Finally, the slope of the fit lines to ΔL varies between the data, with the northern hemisphere plots of By having a positive slope for the IMAGE data and the equatorward OpenGGCM boundary but a negative slope for all of the other models. The slopes of the ΔL versus By plots in the southern hemisphere are positive for all models and the satellite data (except for 0 correlation fits).

18.5. DISCUSSION

ΔL measured from POLAR and IMAGE correlated best with a 30-min average of By, a 45-min average of θ_C, and a 50-min average of ε. An initial conclusion is to think the magnetosphere responds to each of these variables

on those time scales, but a deeper look into the solar wind data shows this is not the case. The first thing to note is how high the By component is, ranging from 22 nT to 32 nT, with an average of 28 nT over the course of the event. In comparison, the only other studies of conjugate aurora captured by POLAR and IMAGE occurred during events with By between −10 nT and 10 nT [*Reistad et al.,* 2013]. This abnormally high By, coupled with the fact that we only examined 67 images taken over a 2-1/2-hour interval means we do not have a firm basis for drawing broad conclusions.

We also do not have evidence to support ΔL responding specifically to one parameter. When looking at 45-min averaged solar wind parameters, we find By, Bz, θ_C, and the ε parameter all show high correlations ($0.8 < r < 0.9$) with ΔL. However, the 1-min and 45-min averaged parameters are all highly collinear for this event. To draw any conclusions about which solar wind parameter has the strongest effect on the Dawn-Dusk Offset, we would need to add to our study other events where the solar wind data have a larger range of values. Additionally, the dipole tilt angle influences auroral symmetry but is not observed in a two-hour long event [*Østgaard,* 2005; *Liou and Newell,* 2010]. Future studies would greatly benefit from examining several events, and thus, looking at a larger parameter space.

18.5.1. Lobe Cells

The largest source of error in locating the satellite imaged PCB occurs at dusk in the northern hemisphere near the end of the event (Figure 18.1). The difficulty arises from weak precipitation occurring well inside the main auroral oval. If we look at the ionosphere computed by BATS-CRCM (Figure 18.2), we see a southern hemisphere with two convection cells of comparable strength, and the PCB running through the middle of each cell. However, the northern hemisphere has a dominant dusk convection cell sitting inside the polar cap boundary. BATS-R-US has similar ionospheric convection, and the LFM and OpenGGCM models also show dominant dusk convection cells sitting inside the PCB. A convection pattern like this in the summer hemisphere during a strong + By period is best explained by a lobe cell circulating within the dusk convection cell [*Burch et al.,* 1985].

A lobe cell arises when the IMF merges not with a dayside closed magnetic field line but with a field line in the tail that is already open, leading to a "stirring" of open field lines [*Reiff et al.,* 1985]. A lobe cell can be completely open, or partially open and partially closed, depending on the tilt of the dipole and the x-component of the IMF [*Crooker and Rich,* 1993]. This process may be fundamentally unstable, thus, the difficulty in the models in successfully tracing the open/closed boundary could be related to the existence of these lobe cells. However, it is also possible the difficulties the models had could be due to the grid size they were run on, as shown in *Ridley et al.* [2010], or by other features inherent to the models. Another potential source of disagreement may be the use of a relatively low precipitation flux as the operational definition of the PCB in the images. Using a significantly higher flux level as the operational definition of PCB can move it to lower latitudes, below the area we have tentatively identified as lobe cells. However, with that definition, the correlation of those boundaries with the IMF is not as good. These will be examined in a follow-up paper.

18.5.2. Model Validity

The unusually high By during this event allows us to test the robustness of the models used. While ΔL measured by IMAGE and POLAR correlated well with all the time-averaged solar wind parameters, only the northern hemisphere of the BATS-R-US and BATS-CRCM models showed comparable correlations. In the southern hemisphere, the observed correlation with By was opposite to that expected from any model, and is likely to be strongly aliased by the time variation of Bz along with By. The LFM model was also the only model to calculate average ΔL values in the same range as IMAGE and POLAR, with the ranges of BATS-R-US and BATS-CRCM being too narrow, and the range of OpenGGCM showing strong variability.

The BATS-R-US and BATS-CRCM generated outputs that are too symmetric compared to the satellite observations. The LFM model generated polar cap boundaries that are distorted and asymmetric but generally in line with the observed polar cap measurement. The OpenGGCM model predicted highly irregular polar cap boundaries. The most critical zero-level predictions are the average Dawn-Dusk Offset and the range of the offsets during the event, which clearly show the LFM model producing an average polar cap offset closest to the observed polar cap offset (Table 18.3). The BATS-CRCM and LFM models are coupled with an inner magnetosphere model, which could explain the better performance of BATS-CRCM compared to the BATS-R-US model, and the overall better performance of the LFM model.

18.6. SUMMARY

Using the Dawn-Dusk Offset as a proxy measurement of auroral conjugacy, we have found each hemisphere responds differently to changes in the solar wind. The northern (summer) hemisphere develops a lobe cell within the dusk convection cell, creating a moderate amount of precipitation not seen in the southern hemisphere. Even before the lobe cell occurs, we see a trend where the Dawn-Dusk Offset decreases with time in each hemisphere, causing the southern hemisphere to become more symmetric

about the pole but leading to a greater asymmetry of the northern polar cap. Our observations were compared to several MHD model outputs, with no model yielding an accurate depiction of the event. Most of the disagreement between the models and the satellite data, and between the models themselves, results from the way each model depicted a lobe cell developing throughout the event.

ACKNOWLEDGMENTS

This work was carried out using the SWMF/BATS-R-US tools developed at The University of Michigan Center for Space Environment Modeling (CSEM) and made available through the CCMC. POLAR-VIS data are available from The University of Iowa, and IMAGE WIC data are available from The University of California, Berkley. This research was partially supported by the Magnetospheric Multiscale Mission (MMS) mission under grant 599790Q. More detail can be found in the M.S. thesis of William Longley, [https://scholarship.rice.edu/handle/1911/77212], upon which this paper is based. Videos of the entire auroral conjunction event, and with overlays of the model predicted boundaries, can be seen at http://space.rice.edu/IMAGE/conjunction.

REFERENCES

Burch, J. L., P. H. Reiff, J. D. Menietti, R. A. Heelis, W. B. Hanson, S. D. Shawhan, E. G. Shelley, M. Sugiura, D. R. Weimer, and J. D. Winningham (1985), IMF B_y-dependent plasma flow and Birkeland currents in the dayside magnetosphere: 1. Dynamics Explorer observations, *J. Geophys. Res.*, *90*(A2), 1577–1593, doi:10.1029/JA090iA02p01577.

Burch, J. L. (2000), Image mission overview, *Space Science Reviews*, *91*, 1–14.

Crooker, N. U., and F. J. Rich (1993), Lobe cell convection as a summer phenomenon, *J. Geophys. Res.*, *98*(A8), 13,403–13,407, doi:10.1029/93JA01037.

Frank, L. A., J. B. Sigwarth, J. D. Craven, J. P. Cravens, J. S. Dolan, M. R. Dvorsky, P. K. Hardebeck, J. D. Harvey, and D. W. Muller (1995), The visible imaging system (VIS) for the Polar Spacecraft, *Space Science Reviews*, *71*, 297–328.

Fuller-Rowell, T. J., et al. (1996), A coupled thermosphere ionosphere model (CTIM), in: STEP Report, R. W. Schunk, ed., Scientific Committee on Solar Terrestrial Physics, NOAA/NGDC, Boulder, CO, *239*.

Glocer, A., M. Fok, X. Meng, G. Tóth, N. Buzulukova, S. Chen, and K. Lin, (2013). CRCM + BATSRUS two-way coupling. *Journal of Geophysical Research: Space Physics*, *118* (4), 1635–1650. doi:10.1002/jgra.50221.

Hapgood, M. A. (1992), Space physics coordinate transformations: A user guide. *Planetary and Space Science*, Vol. *40*, No. 5, pp. 711–717.

Liou, K., and P. T. Newell (2010), On the azimuthal location of auroral breakup: Hemispheric asymmetry, *Geophys. Res. Lett.*, *37*, L23103, doi:10.1029/2010GL045537.

Lyon, J. G., J. A. Fedder, and C. M. Mobarry (2004), The Lyon-Fedder-Mobarry (LFM) global MHD magnetospheric simulation code, *J. Atmos. Solar-Terr. Phys.*, *66*, 1333.

Mende, S. B., et al. (2000), Far ultraviolet imaging from the IMAGE spacecraft. 2. Wideband FUV imaging, *Space Science Reviews*, *91*, 271–285.

Merkin, V. G., and J. G. Lyon (2010), Effects of the low-latitude ionospheric boundary condition on the global magnetosphere, *JGR*, *115*, A10202, doi:10.1029/2010JA015461.

Østgaard, N., N. A. Tsyganenko, S. B. Mende, H. U. Frey, T. J. Immel, M. Fillingim, L. A. Frank, and J. B. Sigwarth (2005), Observations and model predictions of substorm auroral asymmetries in the conjugate hemispheres, *Geophys. Res. Lett.*, *32*, L05111, doi:10.1029/2004GL022166.

Powell, K. G., P. L. Roe, T. J. Linde, T. I. Gombosi, and D. L. De Zeeuw (1999), A Solution-Adaptive Upwind Scheme for Ideal Magnetohydrodynamics Journal of Computational Physics, Volume 154, Issue 2, 20 September, Pages 284–309, 10.1006/jcph.1999.6299.

Pulkkinen, A., L. Rastätter, M. Kuznetsova, H. Singer, C. Balch, D. Weimer, G. Tóth, A. Ridley, T. Gombosi, M. Wiltberger, J. Raeder, and R. Weigel (2013), Community-wide validation of geospace model ground magnetic field perturbation predictions to support model transition to operations. *Space Weather*, *11*(6), 369–385. doi:10.1002/swe.20056.

Raeder, et al. (2001), Global simulation of the geospace environment modeling substorm challenge event, *JGR*, *106*, 381.

Reiff, P. H., and J. L. Burch (1985), IMF B_y-dependent plasma flow and Birkeland currents in the dayside magnetosphere: 2. A global model for northward and southward IMF, *J. Geophys. Res.*, *90*(A2), 1595–1609, doi:10.1029/JA090iA02p01595.

Reiff, P. H., H. L. Collin, J. D. Craven, J. L. Burch, J. D. Winningham, E. G. Shelley, L. A. Frank, and M. A. Friedman (1988), Determination of auroral electrostatic potentials using high- and low-altitude particle distributions, *J. Geophys. Res.*, *93*(A7), 7441–7465, doi:10.1029/JA093iA07p07441.

Reistad, J. P., N. Østgaard, K. M. Laundal, and K. Oksavik (2013), On the non-conjugacy of nightside aurora and their generator mechanisms, J. Geophys. Res. *Space Physics*, *118*, 3394–3406, doi:10.1002/jgra.50300.

Ridley, A. J., Gombosi, T. I., Sokolov, I. V., Tóth, G., and Welling, D. T. (2010). Numerical considerations in simulating the global magnetosphere. *Annales Geophysicae*, *28*(8), 1589–1614. doi:10.5194/angeo2815892010.

Stubbs, T.J., R. R. Vondrak, N. Østgaard, J. B. Sigwarth, and L. A. Frank (2005), Simultaneous observations of the auroral oval in both hemispheres under varying conditions., *Geophys. Res. Lett*., Vol *32*, L03103, doi:10.1029/2004GL021199.

Tóth, G., B. van der Holst, I. V. Sokolov, D. L. De Zeeuw, T. I. Gombosi, F. Fang, W. B. Manchester, X. Meng, D. Najib, K. G. Powell, Q. F. Stout, A. Glocer, Y.-J. Ma, M. Opher (2012), Adaptive numerical algorithms in space weather modeling. *Journal of Computational Physics*, *231* (3), 870–903. doi:10.1016/j.jcp.2011.02.006.

VanZandt, T. E., W. L. Clark, and J. M. Warnock (1972), Magnetic apex coordinates: A magnetic coordinate system for the ionospheric F_2 layer, *J. Geophys. Res.*, *77*(13), 2406–2411, doi:10.1029/JA077i013p02406.